photonics

MDPI

Communication

Multimode, Aperiodic Terahertz Surface-Emitting Laser Resonators

Simone Biasco [1], Lianhe Li [2], Edmund H. Linfield [2], A. Giles Davies [2] and Miriam S. Vitiello [1,*]

[1] NEST, CNR—Istituto Nanoscienze and Scuola Normale Superiore, Piazza San Silvestro 12, 56127 Pisa, Italy; simone.biasco@sns.it

[2] School of Electronic and Electrical Engineering, University of Leeds, Leeds LS2 9JT, UK; l.h.li@leeds.ac.uk (L.L.); E.H.Linfield@leeds.ac.uk (E.H.L.); G.Davies@leeds.ac.uk (A.G.D.)

* Correspondence: miriam.vitiello@sns.it; Tel.: +39-050-509-791

Received: 5 April 2016; Accepted: 16 May 2016; Published: 20 May 2016

Abstract: Quasi-crystal structures are conventionally built following deterministic generation rules although they do not present a full spatial periodicity. If used as laser resonators, they open up intriguing design possibilities that are simply not possible in conventional periodic photonic crystals: the distinction between symmetric (vertically radiative but low quality factor Q) and anti-symmetric (non-radiative, high Q) modes is indeed here fully overcome, offering a concrete perspective of highly efficient vertical emitting resonators. We here exploit electrically pumped terahertz quantum cascade heterostructures to devise two-dimensional seven-fold quasi-crystal resonators, exploiting rotational order or irregularly distributed defects. By lithographically tuning the lattice quasi-periodicity and/or the hole radius of the imprinted patterns, efficient multimode surface emission with a rich sequence of spectral lines distributed over a 2.9–3.4 THz bandwidth was reached. We demonstrated multicolor emission with 67 mW of peak optical power, slope efficiencies up to ≈70 mW/A, 0.14% wall plug efficiencies and beam profile results of the rich quasi-crystal Fourier spectrum that, in the case of larger rotational order, can reach very low divergence.

Keywords: Terahertz; quantum cascade lasers; quasi-crystals

1. Introduction

Two-dimensional (2D) photonic structures have been widely investigated in recent years, since they can be intriguingly engineered to accurately control the optical properties of passive or active devices such as optical fibers [1], waveguides [2] or lasers [3–5] over a broad frequency range, from the visible to the far-infrared. The use of integrated photonic structures to tailor the behavior of light is, indeed, extremely promising for optimizing performance and for introducing advanced functionalities into photonic and optoelectronic devices.

Bi-dimensional semiconductor photonic crystal lasers usually rely on an optically pumped central area, surrounded by un-pumped absorbing regions. More recently, the same concept has been translated to the more appealing electrically pumped photonic crystal laser structures, which exploit quantum cascade laser (QCL) active regions. Laser action has been demonstrated at mid-IR [6] and terahertz (THz) frequencies [7] providing a fascinating solution for the achievement of simultaneous spectral and spatial (surface emission and beam shaping) mode engineering [8–10].

In a photonic crystal QCL, operation is normally achieved on modes at the edges of photonic bandgaps [11] or on the localized states formed by suitably designed defects [12] within the periodic photonic lattice. This implies that efficient vertical out-coupling is typically hindered by the symmetry of the lasing modes, which usually leads to power cancellation in the far-field. This issue can be circumvented by using quasi-crystal patterns ([13,14]), in which the distribution of the dielectric scatterers deviates from periodicity while still being governed by a deterministic generation rule.

Quasi-crystals [15] possess optical properties lying between those of periodic photonic crystals and those of random arrangements of scatterers: on one side, they support extended band-like states with pseudo-gaps in the energy spectrum, on the other, lacking translational invariance, they also intrinsically feature a pattern of "defects" which can give rise to critically localized modes, similar to Anderson modes in random structures [16].

Very differently from the case of photonic crystals, a band description fails in a quasi-crystal, owing to the lack of translation invariance. However, its Fourier structure S(k) [17] can be exploited in a laser cavity to engineer the mode frequency and spacing separately, or to control the emission profile independently of the feedback conditions. S(k) indeed encodes the long-range symmetry of the quasi-crystal, providing a clear indication on the main Bragg reflection processes. These features can be exploited in a laser cavity to give rise to a rich emission spectrum, to control the frequency spacing, to increase the intra-cavity field and to simultaneously shape the far-field intensity profile.

The first reports of optically pumped quasi-crystal lasers are in the visible range [18]. More recently, we devised the first single-mode quasi-crystal electrically pumped THz QCL [19], exploiting a double-metal waveguide configuration and a Penrose tiling of pentagonal rotational symmetry. By manipulating *ad hoc* the photon wave-vectors, the quasi-crystal resonators offer an interesting perspective for the implementation of photonic devices exploiting a large sequence of high quality factor (Q) optical modes.

Here we report on the development of seven-fold quasi-crystal QCL resonators, conceived with two different architectures: a seven-fold rotationally-invariant quasi-crystal design and a graded geometry with irregularly distributed defects. Among the broad range of conceivable seven-fold architectures, we selected two prototypical patterns providing a large sequence of high Q optical modes spanned over a ~500 GHz frequency range. Multimode emissions with up to 10 spectral lines around a central frequency of 3.1 THz have been achieved, with an average peak power of ~70 mW and beam divergence <15°.

2. Design and Simulations

The selected QCL heterostructure was sandwiched between two metallic cladding layers to create a double-metal waveguide which confines, with an almost unitary confinement factor, the THz radiation in the direction of growth (vertical, *z*-axis) and allows its propagation in the *x*–*y* plane, therefore making the device a nearly ideal 2D photonic system. To implement the desired quasi-crystal geometries, holes were opened in the top metallization of a mesa structure, at the vertices of the selected tiles. Photons can be scattered there by the imprinted circular regions which exploit high-refractive-index contrast with the surrounding material, and then vertically extracted when their in-plane momentum is reduced to zero.

The exploited quasi-crystal patterns have been computer-generated with a MATLAB code, implementing the generalized dual method (GDM) [20]. The latter algorithm allows generating quasi-crystal structures with arbitrary orientation order. In the present case, we defined a 2π/seven-rotation invariance around the center of the pattern. The code parameters have been subsequently tuned to add some localized defect points, in order to explore the effects of a high degree of disorder in the devised structures. To this aim, we explored two different geometries: a seven-fold rotationally invariant pattern (type A) and a low-symmetry seven-fold architecture with localized defect points (type B). Each pattern has been characterized via the quasi-crystal average inter-site distance a and the radius r of the open holes, which define the related filling factor FF = r/a. FF has been varied here in the 23%–30% range to ensure the reasonable optical confinement needed to have high gain and sufficient extraction of light from the devices [9,10,19].

The overall device surface area has been set in the range of 0.53–0.64 mm^2 in order to allow a proper balance between the total dissipated electrical power and surface-related diffractive effects.

A commercial finite element (FEM) solver was used to compute the eigenvalue solutions to Maxwell's equations for our 2D system, after assuming the structure is invariant along the *z*-axis and

represented by an equivalent crystal composed of two materials with different local effective dielectric constants (one for the regions comprising the holes, and one for the un-patterned area).

The surrounding region is then modeled as an absorbing layer, leading to smooth boundary conditions for the guided modes. A full 3D simulation was finally performed to have access to the radiative quality factor ($Q_{vertical}$) and to validate the predictions of the 2D model.

Effective dielectric constants were calculated by solving the Helmholtz equation for an infinite slab waveguide with and without top metallization, giving effective refractive indexes $n_1 = 3.6$ and $n_2 = 2.7$ in the metallized and non-metallized regions, respectively. This approximation may seem rather crude for a patterned device, as the fields are no longer uniform in the vertical direction due to the presence of the apertures [21]. Indeed, it is known that it induces deviations in the calculation of the eigenfrequencies; nonetheless, it gives a good qualitative representation of the existing modes and their symmetries. The 2D simulations were performed after defining a surrounding domain with complex effective index $n_3 = 3.6 + 0.36i$, which was used to model the absorbing layer, providing smooth boundary conditions for the guided modes. Finally, an external domain having $n_4 = 1.0$ and scattering boundary conditions (SBC) was used to model the open boundaries outside the mesa. The three-dimensional (3D) model was conversely performed by considering the top and bottom metallization as perfect electric conductors (PECs). The etched GaAs/AlGaAs QCL heterostructure with the thin (7 nm) absorbing Cr border has been treated as a Cr-surrounded 10-μm-thick GaAs slab with a uniform refractive index of $4.43 + 0.31i$. The thin chromium border allows suppressing any Fabry-Perot or whispering gallery mode. The SBC set over the air domain around the resonator mimic light out-coupling to the free space. A schematic diagram of the simulated device is shown in Figure 1.

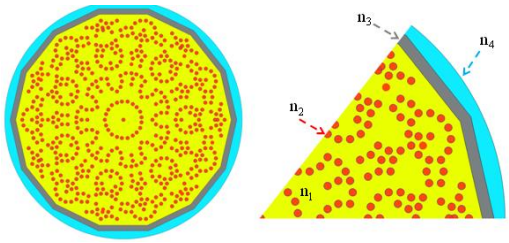

Figure 1. Simulated tetradecagonal mesa geometry with the main dielectric area having refractive index $n_1 = 3.6$, filled by circular scatters having refractive index n_2. A surrounding region with a 35 μm width and a complex effective index of $n_3 = 3.6 + 0.36i$ was used to model the absorbing layer, defining smooth boundary conditions for the guided modes. An external region, having $n_4 = 1.0$ and being terminated by scattering boundary conditions, was used to model the open boundaries outside the mesa device.

Resonating eigenfrequencies, quality factors (Q), and TM spatial profiles for the photonic modes were numerically obtained from the eigenvectors and complex eigenvalues of the FEM model.

The bi-dimensional quality factor (Q_{2D}), which accounts only for the lateral mode confinement, without including the out-of-plane radiative losses, was initially simulated to provide indication of the effects of the filling factor on the scattered light intensity. Modes with higher Q factors can here arise only from a reduced overlap with the outer absorbing boundary, *i.e.*, from a spatial distribution mainly localized in the device center; these modes are therefore the principal ones confined by the grating feedback.

3. Results and Discussion

We therefore varied *a* in the range of 29.9–32.5 μm, *r* in the range of 7.1–9.2 μm while keeping FF in the range of 23%–30% for type A devices, and *a* in the range of 28.5–30.0 μm, *r* in the range of 7.0–8.2 μm while keeping FF unchanged (23%–30%) for type B devices. The scanning electron

microscope images of prototypical type A and type B resonators are shown in Figure 2a,b, respectively, together with the related form factors (Figure 2c,d).

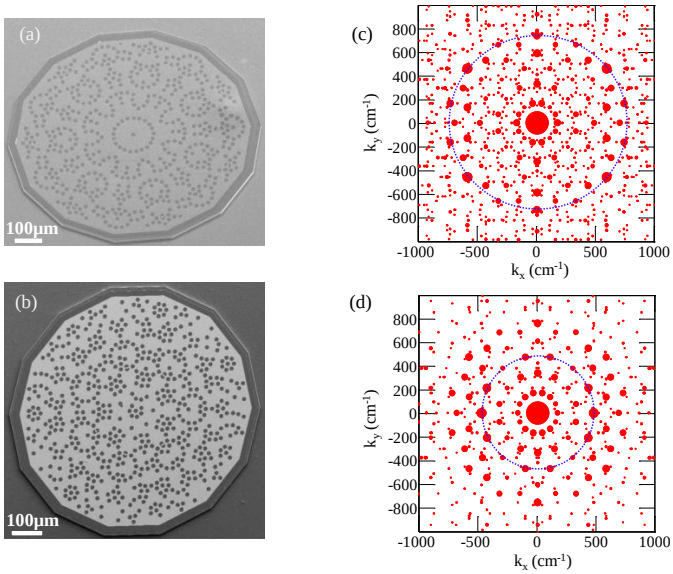

Figure 2. (**a**) Scanning electron microscope (SEM) image of one of the fabricated type A resonators, with a hole radius r = 8.0 μm, average intersite distance a = 29.9 μm and area 0.53 mm^2; (**b**) SEM image of one of the prototype type B resonators, with r = 7.5 μm, a = 30.0 μm and area 0.53 mm^2; (**c**,**d**) Form factor S(k) of the type A (**c**) and type B (**d**) quasi-crystals. The red spots indicate the reciprocal vectors, with radii proportional to associated squared Fourier coefficients. The blue circles of radius k_p show Bragg peaks of S(k) responsible for vertical extraction.

For type A devices, a large number of eigenmodes with $Q_{2D} > 200$ can be found (Figure 2a) over a scattered background of low-Q_{2D} (mean value $Q_{2D} = 125 \pm 34$) optical modes. Conversely, the defect quasi-crystal type B geometry shows a less scattered Q_{2D} frequency distribution, with maximum values in the 150–180 range (Figure 3a). The more regular pattern architecture in the designed type A quasi-crystals induces an enhanced confinement of a few optical modes in the QCL resonator cavity, which is nicely reflected in the form factor S(k) (Figure 2c), which shows a few sharp peaks.

Conversely, in the case of type B quasi-crystals the Fourier spectrum features more reciprocal vectors with comparable amplitude. A large number of Bragg peaks appear on concentric circles with different radii, with an angular separation of $\pi/7$. They have almost the same square Fourier coefficients, indicating they can equally contribute to the scattering mechanisms, very differently from the case of type A resonators, where a smaller number of intense reciprocal vectors is visible. Independently of the device size and the defect distribution, the geometries with intermediate FF (in the range of 24%–28%) sustain a significant number of coexisting high Q_{2D} modes, lying in the spectral region of 2.9–3.4 THz.

The calculated 2D spatial profiles of the high Q_{2D} modes A,B,C and D,E,F, represented by the modulus of the electric field component in the vertical (z) direction, are reported in Figure 3b–d and Figure 4b–d, respectively, and provide an initial indication of the possible Bragg peaks responsible for the feedback [19]. Standing waves form in the crystal as a consequence of multiple diffractions on the main reciprocal lattice points, according to the relation $\Sigma\,(\mathbf{k} - \mathbf{K_j}) = 0$, where $\mathbf{K_j}$ are reciprocal lattice Bragg points and $\mathbf{k}$ is the optical mode wavevector.

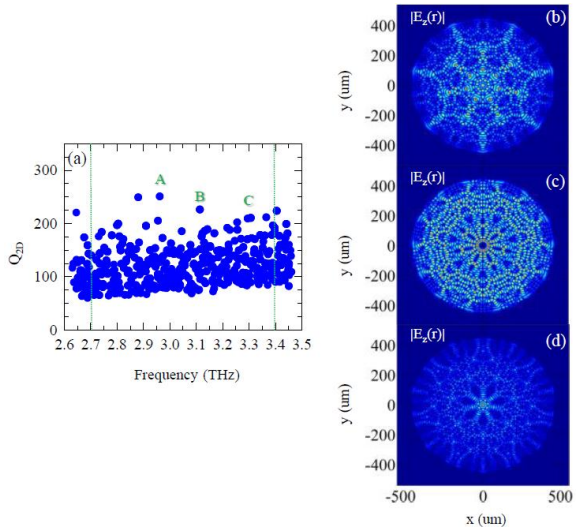

Figure 3. (**a**) Quality factor Q of the computed optical modes as a function of the radiation frequency for a seven-fold (type A) resonator with r = 8.0 μm and a = 29.9 μm. Green vertical lines indicate the employed QCL gain bandwidth; (**b**–**d**) Computed 2D spatial profiles of the electric field modulus for the higher Q optical modes of Figure 2a: (**b**) A; (**c**) B; and (**d**) C.

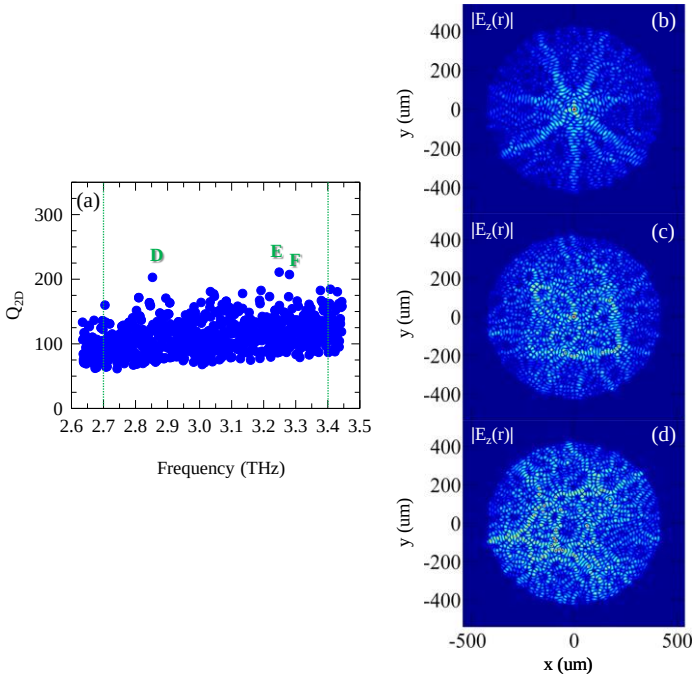

Figure 4. (**a**) Quality factor Q of the computed optical modes as a function of the radiation frequency for a seven-fold (type B) quasi-crystal resonator with r = 7.6 μm, a = 30.0 μm. Green vertical lines indicate the QCL gain bandwidth; (**b**–**d**) Computed 2D spatial profiles of the electric field modulus for the higher Q optical modes of Figure 3a: (**b**) A; (**c**) B; and (**d**) C.

A set of resonators, for each type of architecture, was realized via a combination of optical lithography and metal deposition. The six resonators with type A geometry were engineered with the following parameters: four of them exploited a = 29.9 μm and different hole radius to get FF = 23.7%, 24.4%, 26.8% and 28.1%, respectively; two devices exploit an increased a = 32.5 μm and a radius varied to keep FF unchanged from the maximum values of the previous sample batch, *i.e.*, FF = 26.8% and

28.1%. In the case of the defect type B quasi-crystals, the five resonators have FF = 23.3%, 25.0%, 27.0%, (with fixed a = 28.8 μm) and FF = 23.3%, 25% with a = 30.0 μm.

In order to exploit the large number of computed high Q_{2D} modes and achieve multicolor emissions, we selected as an active medium a hybrid bound-to-continuum QCL design combined with a single-quantum-well phonon extraction stage [22], characterized by a 700 GHz gain bandwidth, extending from 2.7 THz to 3.4 THz.

Figure 5a,b show the measured current density-voltage (J-V) and power-current density (L-J) characteristics of the six type A quasi-crystals QCLs, collected while driving the resonators in pulsed mode at 10 K with a 1% duty cycle. The threshold current density (J_{th}) strongly depends on the photonic-quasi-crystal characteristics providing an initial indication that different optical modes are active, depending on the applied boundary conditions. Specifically J_{th} progressively increases at large FF and varies between 400 A/cm^2 and 450 A/cm^2. Furthermore, by increasing a and keeping fixed FF, a further J_{th} increase is induced, as shown from the comparison between panel 5a and 5b.

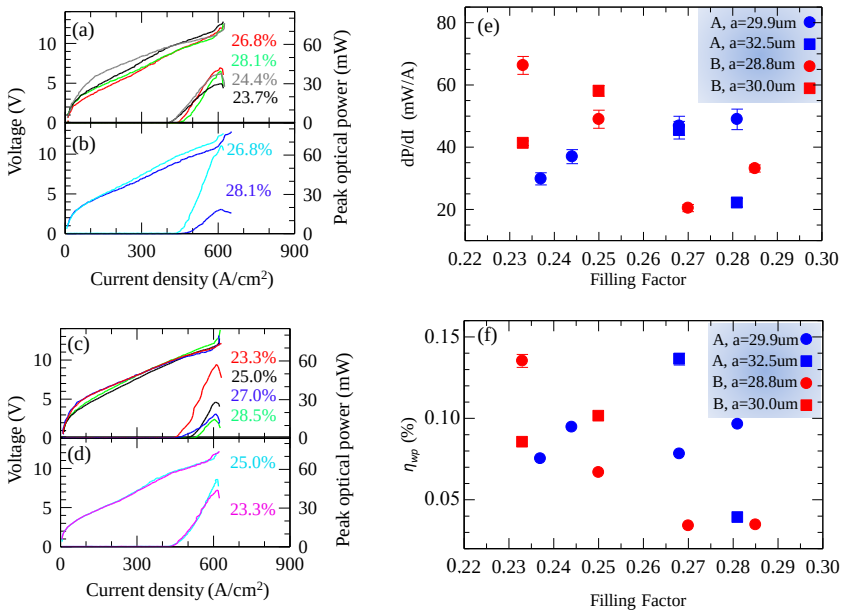

Figure 5. (**a**–**d**) Power current density (LJ) and voltage current density (VJ) characteristics measured at 10 K, in pulsed mode with a 1% duty cycle, for the whole set of fabricated type A (**a**,**b**) and type B (**c**,**d**) resonators. Panel (a) refers to a type A resonator with a = 29.9 μm, panel (b) to a type A resonator with a = 32.5 μm, panel (c) to a type B resonator with a = 28.8 μm and panel (d) to a type B resonator with a = 30.5 μm. Optical power scales have been corrected to take into account the detector collection efficiency and the absorption of the cyclic olefin copolymer cryostat window; (**e**,**f**) Slope efficiency dP/dI (**e**) and wall-plug efficiency η_{WP} (f) plotted as a function of the filling factor. Red symbols refer to type B samples having a = 28.8 μm (•) and a = 30.0 μm (▪); blue symbols refer to type A samples with a = 28.8 μm (•) and a = 30.0 μm (▪).

Figure 5c,d show the L-J-V plot of the six type B defect quasi-crystal resonators, collected under identical experimental conditions. The measured J_{th} vs FF trend follows the same behavior observed in type A resonators, with slightly larger values in the range J_{th} = 450–530 A/cm^2. However, differently from the previous case, a further lattice constant a increase at fixed FF (Figure 5d) induces a J_{th} reduction.

In both sets of samples, remarkable peak optical power values were reached with a maximum of ≈ 67 mW for FF = 26.8% in a type A device and ≈ 60 mW for FF = 23.3% in a type B resonator. The vertical out-coupling is strongly affected by the implemented photonic structures, showing a clear dependence of the quasi-crystal pattern hole radius and the FF values. However, the behaviors of the

type A and defect type B quasi-crystals are quite different. When the type A architecture is adopted, the peak optical power and the slope efficiency *dP/dI* (Figure 5e) progressively increase as a function of FF and then of *r* when *a* is kept constant at 29.9 μm, as an effect of the better vertical out-coupling in large-hole resonators. However, when both *a* and *r* are further increased (see comparison between Figure 5a,b), *dP/dI* shows a dramatic drop with FF, since different optical modes showing different losses and confinement factors start to become active. Conversely, in the case of the defect quasi-crystal type B resonators, the optical power progressively decreases with FF when a = 28.8 μm, while the slope efficiency (Figure 5e) shows a minimum around FF = 27%; by further increasing a = 30.0 μm, the optical power and the slope efficiency start to increase again with *r*, reaching ~70 mW/A as an effect of the stronger scattering strength and thus the better in-plane optical confinement.

Although the power slope efficiency is a figure of merit that relates directly to the radiative Q_{vert} of the implementing resonators, the wall-plug efficiency (η_{WP}) is commonly a very practical parameter to take into account.

Usually in a symmetric photonic-crystal laser, which operates on the band-edge states of the photonic band structure, the modes can be classified as symmetric or anti-symmetric, according to the spatial symmetry of their transverse electromagnetic field components. These two classes of modes have similar cavity losses, but significantly different radiation losses. They are therefore indicated as non-radiative (antisymmetric) and radiative (symmetric) modes. Antisymmetric modes are usually weakly radiative in finite-sized resonators, with low out-coupling efficiencies. In contrast, constructive interference generally occurs for symmetric modes, leading to highly efficient out-coupling. However, non-radiative modes are typically favored for lasing, because of their lower total losses, and usually lead to very low η_{WP} ~ 0.01%. Figure 5f shows the measured η_{WP} in our set of quasi-crystal resonators. Both type A and type B architectures allow reaching η_{WP} = 0.14%, which is comparable with standard double-metal Fabry-Perot resonators.

Emission spectra have been collected in rapid scan acquisition mode via Fourier transform infrared spectroscopy (FTIR) with a resolution of 0.125 cm^{-1}. Figure 6a–d show the set of spectra collected in the type A and type B resonators, respectively, at current values corresponding to the peak optical power. Multimode emission with a maximum of 10 spectral lines spread over a 430 GHz bandwidth is achieved for type A quasi-crystals (Figure 6b). The mode number and related intensities are highly dependent from the different geometrical parameters, resulting in an uneven amplification of the allowed modes in the photonic structures. In the case of defect mode type B quasi-crystals, the highest number of amplified modes (six) is obtained for the lowest FF = 23.3% and FF = 25% and for the larger lattice quasi-periodicity (Figure 6d). In all cases, the frequency spacing between adjacent modes cannot be attributed to Fabry-Perot-like or whispering gallery modes, due to the absorbing boundary created by the outer chromium border.

The spectral distribution is in good agreement (with a few tens of GHz discrepancy) with the prediction of the 2D simulations (Figures 3a,b and 4a,b) with the exception of a few modes distributed on the tails of the QCL gain bandwidth. Full 3D simulations were furthermore performed to provide a more accurate description of the modes propagating in the devised resonators, taking the radiative losses into account. The plot of the 3D quality factor (Figure 6e,f), indicates that a few dominant high Q_{3D} optical modes are present, which are indeed responsible for the emitted laser lines of the corresponding resonators (Figure 6b–d), within a <2% frequency discrepancy.

To finally investigate the optical beam emission profile of the fabricated resonators, we collected the far-field intensity distribution by scanning a pyroelectric detector in the *x*–*y* plane, along the surface normal direction. Figure 7a shows the far-field intensity distribution of a type A device with FF = 26.8% and a = 32.5 μm. The beam shape is concentrated in a 15° divergent optical spot. Conversely, the far-field intensity profile of a prototype type B laser (FF = 25.0%, a = 30.0 μm) (Figure 7b) is spread over a 30° divergent optical cone, reflecting the more disordered mode distribution in the resonator and the largest number of Bragg peaks which can provide feedback via a larger number of different wave-vectors.

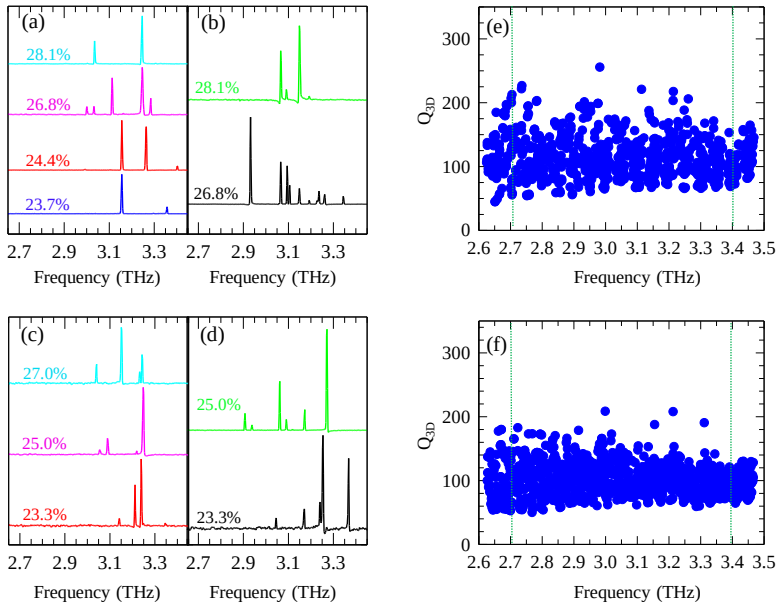

Figure 6. Emission spectra of type A (**a**,**b**) and type B (**c**,**d**) quasi-crystal lasers collected via an Fourier transform infrared spectrometer in rapid scan acquisition mode at 10 K while driving the QCLs with a 1% duty cycle. Panel (a) refers to a type A resonator with a = 29.9 µm, panel (b) to a type A resonator with a = 32.5 µm, panel (c) to a type B resonator with a = 28.8 µm and panel (d) to a type B resonator with a = 30.0 µm; (**e**) Q-factor of the computed optical modes as a function of the radiation frequency for a seven-fold (type A) resonator with r = 8.0 µm and a = 29.9 µm; (**f**) Q-factor of the computed optical modes as a function of the radiation frequency for a seven-fold (type B) quasi-crystal resonator with r = 7.5 µm, a = 30.0 µm. Green vertical lines indicate the QCL gain bandwidth.

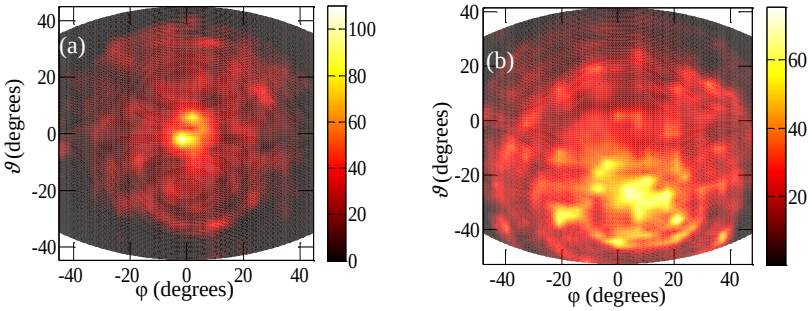

Figure 7. (**a**,**b**) Far-field emission patterns of the (**a**) type A (FF = 26.8%, a = 32.5 µm) and (**b**) type B (FF = 25%, a = 30 µm) obtained by scanning a pyroelectric detector at a distance of about 5 cm distance from the device surface.

We finally characterized the temperature performance of our quasi-crystal resonators. Figure 8a shows the L-J-V characteristics of a type A resonator with FF = 26.8%, collected up to a maximum heat sink temperature of T_H = 105 K, which corresponds to a lattice temperature of $T_L \approx$ 111 K [23].

Figure 8b reports the results of the same experiment performed on a type B quasi-crystal with FF = 25.0%, measured up to a maximum lasing temperature of T_H = 110 K (*i.e.*, $T_L \approx$ 116 K). In all cases, the threshold current density increases with the temperature following the phenomenological formula $J_{th} = J_0 \cdot \exp(T/T_0)$, which allows extracting $T_0 = (113 \pm 9)$K for a type A laser (Figure 8c) and $T_0 = (114 \pm 10)$K for a type B device (Figure 8d), demonstrating that the imprinted photonic structures do not significantly modify the device thermal behavior, which indeed matches that of the reference edge emitting double-metal QCL [22].

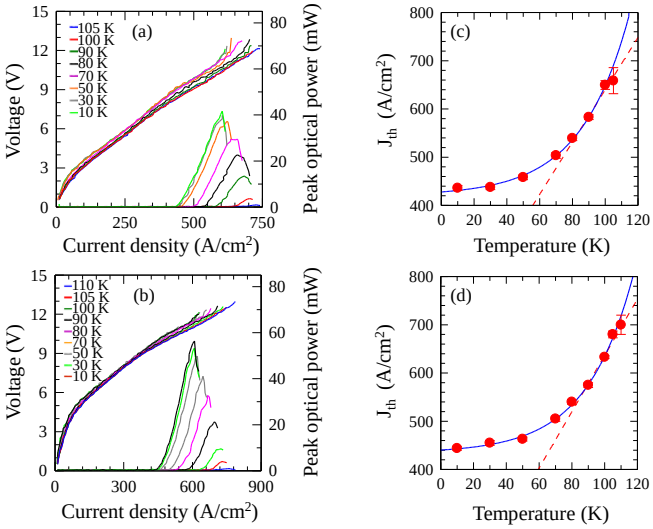

Figure 8. (**a**,**b**) J-V and J-L characteristics of a type A (**a**) (FF = 26.8%), and a type B (**b**) (FF = 25.0%) quasi-crystal, driven at 0.3% duty cycle and different heat sink temperatures; (**c**,**d**) Threshold current density J_{th} as a function of the heat sink temperature for the type A and type B resonators of panels (a) and (b). The blue line represents the fitting function $J_{\text{th}} = J_1 + J_2 \cdot \exp(T/T_2)$, while the dashed line is the linear fit to the data for $T \geqslant 80$ K.

4. Conclusions

Two-dimensional photonic structures based on seven-fold quasi-crystal geometries and exploiting a standard or defect-like configuration were implemented on the top surface of a 2D THz QCL resonator to produce, via lithographic tuning of the imprinted pattern, efficient, multimode surface emissions with a rich sequence of spectral lines distributed over a 2.9–3.4 THz bandwidth, in good agreement with computational predictions. $\geqslant$ 60 mW of emitted peak optical power with slope efficiencies up to $\approx$70 mW/A and η_{WP} = 0.14% have been reached in both configurations, with an optical beam divergence <15°. The demonstrated architecture opens interesting perspectives for the realization of multi-frequency surface-emitting resonators with possible impacts on physical investigations on novel micro-cavity phenomena and related application perspectives on imaging, metrology and optical communications.

Acknowledgments: This work was partly supported by the Italian Ministry of Education, University, and Research (MIUR) through the program IRB—Futuro in Ricerca 2010 RBFR10LULP Fundamental research on Terahertz photonic devices.

Author Contributions: M.S.V. and S.B. devised the concept; S.B. performed the simulations, fabricated the devices and performed the experiments; L.L., E.H.L. and A.G.D., carried out the growth of QCL materials; S.B. and M.S.V. analyzed the data; M.S.V. wrote the manuscript with contributions from the other authors and coordinated the whole project.

Conflicts of Interest: The authors declare no conflict of interest.

Appendix: Fabrication Details

The quantum cascade laser (QCL) was grown by molecular beam epitaxy on an undoped GaAs substrate and consists of a GaAs/$Al_{0.15}Ga_{0.85}As$ heterostructure based on the design reported in Reference [22]. The layer sequence is 5.5/11.0/1.8/11.5/3.8/9.4/4.2/$\underline{18.4}$ (in nm), where $Al_{0.15}Ga_{0.85}As$ layers are in bold, GaAs in Roman, and the underlined number indicates a doped layer with Si with a density of 2×10^{16} cm^{-3}. After growth, the QCL wafer was thermo-compressively bonded with an Au-Au interface on an n^+-GaAs carrier wafer. After selective removal of the host GaAs substrate by etching to and removing the $Al_{0.5}Ga_{0.5}As$ etch-stop layer, the active region was coated with a top Cr/Au (5 nm/150 nm) metallization. Using optical lithographic techniques, holes were imprinted on

this surface, reproducing the quasi-crystal patterns generated by a MATLAB script, implementing the generalized dual method. Two distributions of vertices were designed: one features perfect symmetry under 2π/seven-rotation (type A), the other one is characterized by some defect points increasing the degree of disorder of the system (named type B). In order to implement strong absorbing boundary conditions, the pattern was surrounded by a pre-defined thin Cr (7 nm) frame in the shape of a 14-sided polygon which was placed 30 µm around each photonic structure, partially overlapping with the Au border in order to implement strongly absorbing boundary conditions. This Cr border acted as a mask during the reactive ion etching (RIE) process, preventing the n^+ top contact layer from being etched away at the periphery of the Penrose pattern where the absorbing boundary is required. As a final processing step, decagonal mesa structures were etched down to the bottom metal using an H_2SO_4:H_2O_2:H_2O (11:9:50) etching solution to avoid lateral current spreading. Individual devices were indium soldered onto a copper block and symmetrically wire-bonded around the tetradecagonal border in order to ensure uniform current injection through the mesa, while avoiding any perturbative effects in the far-field.

References

1. Zhao, H.; Zaccaria, R.P.; Verma, P.; Song, J.; Sun, H. Single-mode operation regime for 12-fold index-guiding quasi-crystal optical fibers. *Appl. Phys. B* **2010**, *100*, 499–503. [CrossRef]
2. Jin, C.; Cheng, B.; Man, B.; Li, Z.; Zhang, D.; Ban, S.; Sun, B. Band gap and wave guiding effect in a quasiperiodic photonic crystal. *Appl. Phys. Lett.* **1999**, *75*, 1848–1850. [CrossRef]
3. Meier, M.; Mekis, A.; Dodabalapur, A.; Timko, A.; Slusher, R.E.; Joannopoulos, J.D.; Nalamasu, O. Laser action from two-dimensional distributed feedback in photonic crystals. *Appl. Phys. Lett.* **1999**, *74*, 7–9. [CrossRef]
4. Imada, M.; Noda, S.; Chutinan, A.; Tokuda, T.; Murata, M.; Sasaki, G. Coherent two-dimensional lasing action in surface-emitting laser with triangular-lattice photonic crystal structure. *Appl. Phys. Lett.* **1999**, *75*, 316–318. [CrossRef]
5. Hirose, K.; Liang, Y.; Kurosaka, Y.; Watanabe, A.; Sugiyama, T.; Noda, S. Watt-class high-power, high-beam-quality photonic-crystal lasers. *Nat. Photonics* **2014**, *8*, 406–411. [CrossRef]
6. Colombelli, R.; Srinivasan, K.; Troccoli, M.; Painter, O.; Gmachl, C.F.; Tennant, D.M.; Sergent, A.M.; Sivco, D.L.; Cho, A.Y.; Capasso, F. Quantum cascade surface-emitting photonic crystal laser. *Science* **2003**, *302*. [CrossRef] [PubMed]
7. Chassagneux, Y.; Colombelli, R.; Maineult, W.; Barbieri, S.; Beere, H.E.; Ritchie, D.A.; Khanna, S.P.; Linfield, E.H.; Davies, A.G. Electrically pumped photonic-crystal terahertz lasers controlled by boundary conditions. *Nature* **2008**, *457*, 174–178. [CrossRef] [PubMed]
8. Zhang, H.; Dunbar, L.A.; Scalari, G.; Houdrè, R.; Faist, J. Terahertz photonic crystal quantum cascade lasers. *Opt. Express* **2007**, *15*, 16818–16827. [CrossRef] [PubMed]
9. Chassagneux, Y.; Colombelli, R.; Maineult, W.; Barbieri, S.; Khanna, S.P.; Linfield, E.H.; Davies, A.G. Graded photonic crystal terahertz quantum cascade lasers. *Appl. Phys. Lett.* **2010**, *96*, 031104. [CrossRef]
10. Halioua, Y.; Xu, G.; Moumdji, S.; Li, L.H.; Davies, A.G.; Linfield, E.H.; Colombelli, R. THz quantum cascade lasers operating on the radiative modes of a 2D photonic crystal. *Opt. Lett.* **2014**, *39*, 3962–3965. [CrossRef] [PubMed]
11. Yablonovitch, E. Inhibited spontaneous emission in solid-state physics and electronics. *Phys. Rev. Lett.* **1987**, *58*, 2059–2062. [CrossRef] [PubMed]
12. Park, H.G.; Hwang, J.K.; Huh, J.; Ryu, H.Y.; Lee, Y.H.; Kim, J.S. Nondegenerate monopole-mode two-dimensional photonic band gap laser. *Appl. Phys. Lett.* **2001**, *79*, 3032–3034. [CrossRef]
13. Levine, D.; Steinhardt, P.J. Quasicrystals. I. Definition and structure. *Phys. Rev. B* **1986**, *34*, 596–616. [CrossRef]
14. Socolar, J.E.S.; Steinhardt, P.J. Quasicrystals. II. Unit-cell configurations. *Phys. Rev. B* **1986**, *34*, 617–647. [CrossRef]
15. Vardeny, Z.V.; Nahata, A.; Agrawal, A. Optics of photonic quasicrystal. *Nat. Photonics* **2013**, *7*, 177–187. [CrossRef]

16. Wiersma, D.S. Disordered Photonics. *Nat. Photonics* **2013**, *7*, 188–196. [CrossRef]
17. Matsui, T.; Agrawal, A.; Nahata, A.; Vardeny, Z.V. Transmission resonances through aperiodic arrays of subwavelength apertures. *Nature* **2007**, *446*, 517–521. [CrossRef] [PubMed]
18. Notomi, M.; Suzuki, H.; Tamamura, T.; Edagawa, K. Lasing action due to the two-dimensional quasiperiodicity of photonic quasicrystals with a Penrose lattice. *Phys. Rev. Lett.* **2004**, *92*, 123906. [CrossRef] [PubMed]
19. Vitiello, M.S.; Nobile, M.; Ronzani, A.; Tredicucci, A.; Castellano, F.; Talora, V.; Li, L.; Linfield, E.H.; Davies, A.G. Photonic quasi-crystal terahertz lasers. *Nat. Commun.* **2014**, *5*, 1–7. [CrossRef] [PubMed]
20. Socolar, J.E.S.; Steinhardt, P.J.; Levine, D. Quasicrystals with arbitrary orientational symmetry. *Phys. Rev. B* **1985**, *32*, 5547–5550. [CrossRef]
21. Qiu, M. Effective index method for heterostructure-slab-waveguide-based two-dimensional photonic crystals. *Appl. Phys. Lett.* **2002**, *81*, 1163–1165. [CrossRef]
22. Amanti, M.I.; Scalari, G.; Terrazzi, R.; Fischer, M.; Beck, M.; Faist, J.; Rudra, A.; Gallo, P.; Kapon, E. Bound-to-continuum terahertz quantum cascade laser with a single-quantum-well phonon extraction/injection stage. *New J. Phys.* **2009**, *11*, 125022. [CrossRef]
23. Vitiello, M.S.; Scamarcio, G.; Spagnolo, V.; Alton, J.; Barbieri, S.; Worrall, C.; Beere, H.D.; Ritchie, D.A.; Sirtori, C. Thermal properties of THz quantum cascade lasers based on different optical waveguide configurations. *Appl. Phys. Lett.* **2006**, *89*, 021111. [CrossRef]